THE GEOLOGICAL SOCIETY OF AMERICA®

High-resolution reconstruction of folding history in the central Syrian Arc fold system reveals episodic shortening

Guy Fisch[1,†], Roi Granot[1], Sara Marconato[1], Yehuda Eyal[1], Bar Elisha[2], and Sigal Abramovich[1]
[1]*Department of Earth and Environmental Sciences, Ben-Gurion University of the Negev, Beer Sheva 8410501, Israel*
[2]*Ilse Katz Institute for Nanoscale Science and Technology, Ben-Gurion University of the Negev, Beer Sheva 8410501, Israel*

ABSTRACT

Intraplate shortening of the northern African passive margins has been widely observed, but the history of shortening and thus the underlying processes that led to their reactivation are still poorly understood. Situated at the northeastern African margin, the 1000-km-long Syrian Arc fold system preserves a classic example of such inversion that formed during the closure of the Tethys Ocean. Here, we present new structural and temporal constraints on the evolution of the Hatira monocline, which is situated at the central part of the arc. Our results suggest that intraplate folding was accommodated by a long-term slow background shortening acting since ca. 90 Ma, punctuated by one major folding pulse (ca. 79 Ma to ca. 77 Ma) and two additional relatively subdued pulses (ca. 67 Ma to ca. 65 Ma and ca. 57 Ma to ca. 54 Ma). This intraplate shortening might have been driven by the processes acting along the Africa-Eurasia subduction front (e.g., the secession of a double subduction zone) and/or the dynamic processes acting along the down-going subducting slab (e.g., slab buckling). Our results highlight the need for a new generation of high-temporal resolution plate kinematic models and detailed geodynamical numerical simulations that will link the observed intraplate deformation history with the processes acting along the confining plate boundaries.

INTRODUCTION

The northern African passive margin, initially formed during the opening of the Tethyan oceanic basin from as early as the Carboniferous (Granot, 2016), has experienced several extensional episodes during the Permian, Triassic, and Early Jurassic times (Garfunkel, 2004). The margin extends inland to more than 100 km (Gardosh et al., 2010) and preserves intraplate inversion structures that developed since the Late Cretaceous (Frizon de Lamotte et al., 2011; Guiraud and Bosworth, 1997). One of the most spectacular examples of a well-preserved inversion structure is the Syrian Arc fold system (Krenkel, 1924), a 1000-km-long fold zone straddling the eastern Mediterranean from the Palmyrides, Syria, at the northeast, to Egypt, in the southwest (Fig. 1). While the overall shortening accommodated by the arc is relatively small (up to ∼6 km; Salel and Séguret, 1994), its large spatial extent suggests that large-scale geodynamic processes, rather than local sources, might have induced the stresses that drove its formation.

The Syrian Arc comprises a series of asymmetrical anticlines and synclines that preserve syn- and post-tectonic depositional strata (Reches et al., 1981; Shahar, 1994). Inversion along the arc started in the Late Cretaceous when the African plate was already subducting under the Eurasian plate (Fig. 1B; Hardy et al., 2010). The structural evolution of the region occurred under two main stress fields (Eyal and Reches, 1983). The initial stress field, which operated mainly from the Late Cretaceous to the Eocene at the central part of the arc, had a dominant compressional component trending in a W-WNW direction (present-day coordinates). This stress field was linked to far-field processes, likely related to the processes acting along the northern plate boundary of the African Plate (Gianni et al., 2025). The subsequent stress field, operating since the Miocene, was dominated by an extensional stress component trending in a E-ENE direction. This stress field was linked to the development of the Dead Sea Transform (Eyal and Reches, 1983). Previous structural and sedimentological investigations of the southern and central parts of the arc (i.e., in Sinai and the Negev Desert; Fig. 1) suggested that folding initiated at the Late Turonian, peaked at the Santonian–Campanian, and terminated by the Miocene (Avni, 1989; Moustafa and Khalil, 1995; Salamon, 1987). Seismic and structural observations from Lebanon and the Palmyrides (Fig. 1) imply that the northern part of the arc accommodated shortening during the Late Cretaceous and during the Eocene to Miocene (Chaimov et al., 1992; Walley, 1998). Buried folds at the Levant Basin (Fig. 1), possibly related to the Syrian Arc fold system, have primarily evolved during the Miocene (Sagy et al., 2018). Despite extensive efforts to study the Syrian Arc since the seminal work of Krenkel (1924), due to erosion, depositional hiatuses, and complex folding structures found in most of the onshore folds, obtaining a thorough understanding of the history of folding is challenging and is thus still lacking. Here, we investigate the sedimentary section exposed at the southern part of the Hatira monocline, found at the central part of the arc (i.e., between the Dead Sea Transform and the Levant Basin), southern Israel (Figs. 1 and 2). The exposed section spans the Late Cretaceous to the Eocene, allowing us to study the deformation history at an approximately million-year temporal resolution. Our structural observations and temporal analysis reveal that shortening has developed through a slow and long-lasting shortening interrupted by abrupt and relatively short (∼1 m.y. to ∼3 m.y.) deformational pulses.

Geological Setting of the Hatira Monocline

The Hatira monocline lies in the Negev Desert (Fig. 1). Most of the shortening (i.e., inversion) that led to the creation of the monocline occurred between the Late Cretaceous and the Eocene (Zur, 1997). Still, later regional uplift was recorded up to Miocene times. This young uplift activity phase was linked to the evolution of the Dead Sea Transform (Zilberman, 2024, and references therein). Since the Oligocene, the crest of the monocline has been exposed to erosion, creating an erosional crater along the hinge of the fold, which now exposes a sedimentary

Guy Fisch https://orcid.org/0000-0003-2061-001X
†fischg@post.bgu.ac.il

GSA Bulletin;
Published online 5 November 2025
https://doi.org/10.1130/B38425.1.

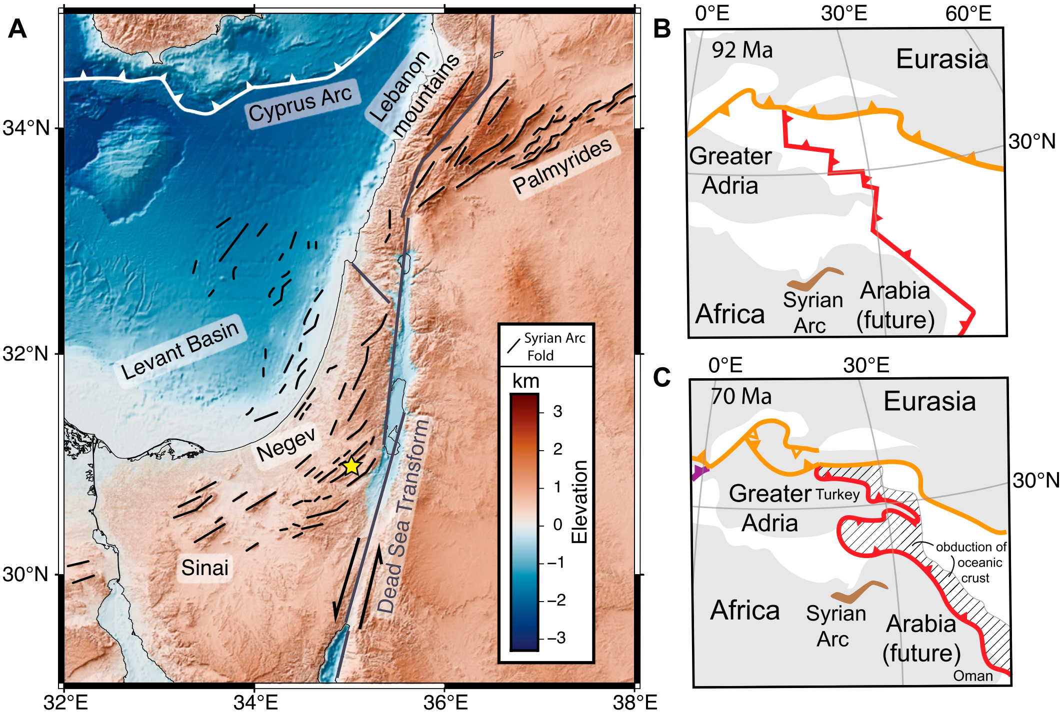

Figure 1. Tectonic and geological framework. (A) An overview map of the Syrian Arc fold system. Black lines highlight the axes of the elongated asymmetrical folds that create the arc (Shahar, 1994). The location of the Hatira monocline is denoted with a yellow star. (B) Simplified plate reconstruction for the Late Turonian (92 Ma; after Gürer et al., 2022) of the study area. (C) Simplified plate reconstruction for the Early Maastrichtian (70 Ma; after Gürer et al., 2022) of the study area.

section of Jurassic to Neogenic rocks (Zilberman, 2024). The monocline extends for 30 km along-strike, reaching a height of 650 m above sea level (Fig. 2). The axis of the monocline is oriented in a northeast-southwest direction, with the northern flank tilted 9° to the northwest, reaching a length of ~7 km. In contrast, the southern flank is sharply tilted (up to ~80°) to the southeast, reaching a length of ~2 km. It is commonly accepted that the Syrian Arc monoclines, with the Hatira monocline among them, formed as fault propagation folds (Reches et al., 1981; Fig. 2B). The monoclines evolved by limb rotation folding driven by reverse motion on preexisting blind normal faults (Salamon, 1987). While most of the faults underlying the monoclines of the Negev Desert, including the Hatira monocline, are not exposed at the surface, several boreholes cutting into the crest of the monoclines, seismic investigations, and structural modeling support this interpretation (Shamir and Eyal, 1995, and references therein). During most of the investigated period, shortening was accommodated while the fold was submerged in the shallow waters of the southern Tethys Ocean (Flexer, 1971); thus, sedimentation along the flanks continued throughout the folding process. Across the steep southern flank of the Hatira monocline (i.e., at the forelimb), a cumulative wedge of growth strata, manifested as a progressive unconformity (Riba, 1976), is exposed at and near the Mador Hill (Figs. 2–4). The wedge is composed of a series of angular unconformities and a decreasing dip magnitude up the section. These syn-tectonic (i.e., syn-shortening) growth strata are truncated by several relatively minor hiatuses (Buchbinder et al., 2000; Meilijson et al., 2014; Fig. 3). Despite the truncation of the upper part of the cumulative wedge, which prohibits a complete analysis of the relations between the growth strata and the forelimb (Fig. 4A), the Mador Hill section unravels the folding history of the monocline through an exposed series of angular unconformities spanning from the Late Cretaceous to the Eocene.

The area surrounding the Mador Hill preserves a Turonian up to Lower Eocene sedimentary section (Roded, 1982) comprised of three lithological groups (Fig. 3). At the investigated section, these three groups comprise an ~200-m-thick lithological sequence, an intermediate thickness between the thin anticlinal and the thick synclinal sequences commonly observed in the central Syrian Arc (Avni, 1989; Soudry et al., 1985). The lower part of the section constitutes the upper Judea Group, represented by the Nezer Formation, composed of Turonian 15-m-thick mixture of mostly fossil-bearing sparitic limestone and some dolomites crossed by calcite veins (Fig. 4B). The Judea Group is regionally truncated and unconformably overlain by the heterogeneous Mount Scopus Group (Flexer, 1968), spanning the Coniacian to the end of the Paleocene. From the Coniacian to the Campanian, this group documents the transition from sedimentation on a carbonate platform to pelagic sedimentation under long-lasting upwelling conditions that acted along the southern continental shelf of Tethys (Almogi-Labin et al., 1993; Meilijson et al., 2014; Soudry et al., 2006). Generally, the group was accumulated under relatively high sedimentation rates (up to 2.7 cm/k.y.; Meilijson et al., 2014). The Paleocene era marks a deepening and transition from shelf to upper bathyal pelagic depositional environment (Ashckenazi-Polivoda et al., 2018). The group is composed of four formations: the Menuha, Mishash, Ghareb, and Taqiye Formations, with a local total thickness of ~170 m. At the base of the Mount Scopus Group is the Coniacian to Early Campanian (Meilijson et al., 2014) Menuha Formation. Only Santonian layers from the Menuha Formation are found at the investigated transect. The formation is composed of hardpacked chalk layers of varying thicknesses (<~11 m), thinning and disappearing completely toward the axis of the anticline (Fig. 4C). Where the Menuha Formation is no longer present, this depositional pattern results in the uncomfortable contact of Campanian and Turonian strata and indicates that folding has ensued before and during the Santonian. The Menuha Formation is overlaid by the Middle Campanian to lowermost Maastrichtian porcellanitic, chert, and phosphorite layers of the Mishash Formation. The porcellanitic and chert member onlaps the Menuha Formation and thins toward the axis of the anticline (Fig. 4D). The phosphorite member (40 m thick) is composed of chalky phosphate rocks, bearing high amounts of organic matter (Fig. 4E). Within this member, a thin (<1 m) breccia layer is pres-

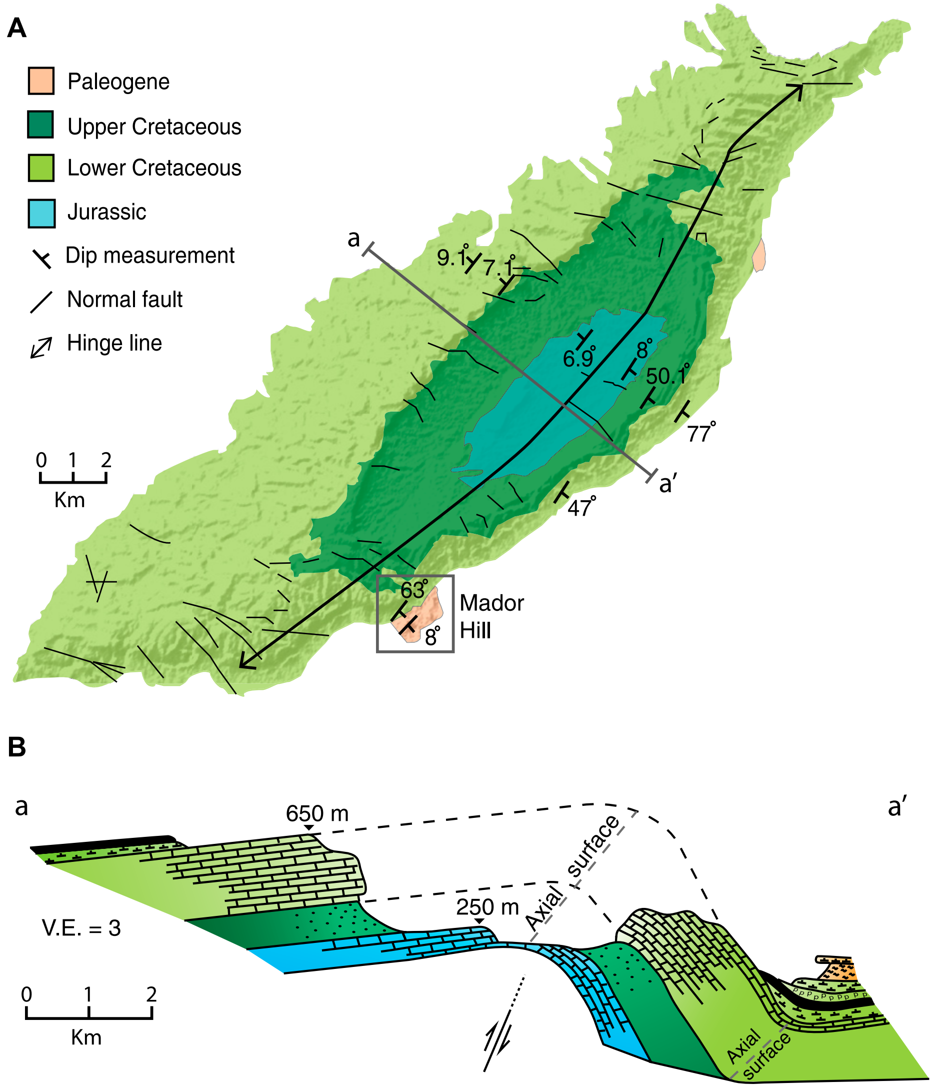

Figure 2. Geological setting of the Hatira monocline. (A) Geological map of the Hatira monocline, modified from Roded (1982). The black a–a′ line denotes the span of the cross section shown in panel B while the gray rectangle highlights the position of Figure 3B. (B) Schematic cross section of the Hatira monocline modified from Zilberman (2024). The cross section has a vertical exaggeration (V.E.) of 3.

ent (inset in Fig. 4E) and is associated with a transition between onlap to offlap sedimentary structure (Fig. 5). The Maastrichtian Ghareb Formation, onlapping the Mishash Formation, is composed of a massive chalk unit followed by a unit of alternating chalk and marl (Fig. 4F). Above the Ghareb Formation, the 70-m-thick Taqiye Formation spans the Paleocene and is composed of fine gray-green marls with limonite concentrations and gypsum veins (Fig. 4G). Its field appearance is of a single massive unit, but fine layering is preserved near the bottom and top of the formation. Finally, the top of the investigated section is represented by the Avedat Group. The contact between the Mount Scopus and Avedat Groups marks the transition from the Paleocene to the Eocene. In the investigated area, the Avedat Group is represented by the Lower Eocene Mor Formation, which is composed of hard-packed chalk rich with glauconite (Fig. 4H). The Mor Formation locally reaches a thickness of 9 m and is truncated at the top by a Quaternary conglomerate (Zur, 1997).

METHODS

Growth strata structures preserve a record of the shortening that occurred during their deposition (e.g., Anastasio et al., 2021; Riba, 1976; Suppe et al., 1992). Under the assumption that any deviation of the sedimentary layers from their original horizontal depositional orientation reflects folding, detailed documentation of their dip magnitude, coupled with biostratigraphic and geochronological dating, should unravel the timing when folding (i.e., shortening) occurred.

We have measured the orientation of the layers with an analog Brunton compass (~2° accuracy) every 2–10 m vertical separation. When the exposure of the layers was poor or overprinted by erosion, the orientation was measured over relatively large exposures (tens of meters) using a Total Station GNSS (Global Navigation Satellite System) sensor (Trimble S6, accounting for ~0.5° accuracy). The orientation of the layers documents the history of folding but is also influenced by other processes. For instance, dip magnitude could be affected by local structural complexities or the distance from the anticlinal axial surface. We have, therefore, identified the influence of the structural setting on the orientation of the layers and corrected the measured orientation whenever necessary (for a detailed description of the structural complexities and corrections, see the Results section).

Our biostratigraphical analysis is based on planktonic foraminifera, benthic foraminifera, and nannoplankton. For foraminiferal analysis, the samples were crushed, soaked in water for two days, then washed through a 63-micron sieve, dried, and scanned for fossils under a Leica M205 C stereomicroscope. Important specimens were further examined by an electron scanning microscope. When carbonate obscured the fossils, the samples underwent ultrasonic treatment to dissolve it. In the final stage of the analysis, we identified biomarkers based on the collected fossils. For nannoplankton analysis, the samples were prepared according to the standard smear-slide technique (Bown, 1998; Bown and Young, 1998) and examined under a Leica DM750P optical microscope with a magnification of 1600×. The Santonian and Campanian foraminifera chronostratigraphies, both benthonic and planktonic, and the Mishash-Menuha Formations transition were adopted from Meilijson et al. (2014). Maastrichtian planktonic foraminifera biozonation was adopted from a Deep Sea Drilling Project study (Li and Keller, 1998), incorporating results from two Atlantic drilling sites. Cenozoic planktonic foraminifera biozones were adopted from chronostratigraphic schemes correlating foraminifera occurrences to the geomagnetic polarity and the astronomical time scales (Berggren et al., 2006; Wade et al., 2011). We have adopted the calcareous nannofossil biozonation of Burnett (1998). The planktonic foraminifera biohorizons and the calcareous nannofossil biohorizons ages origi-

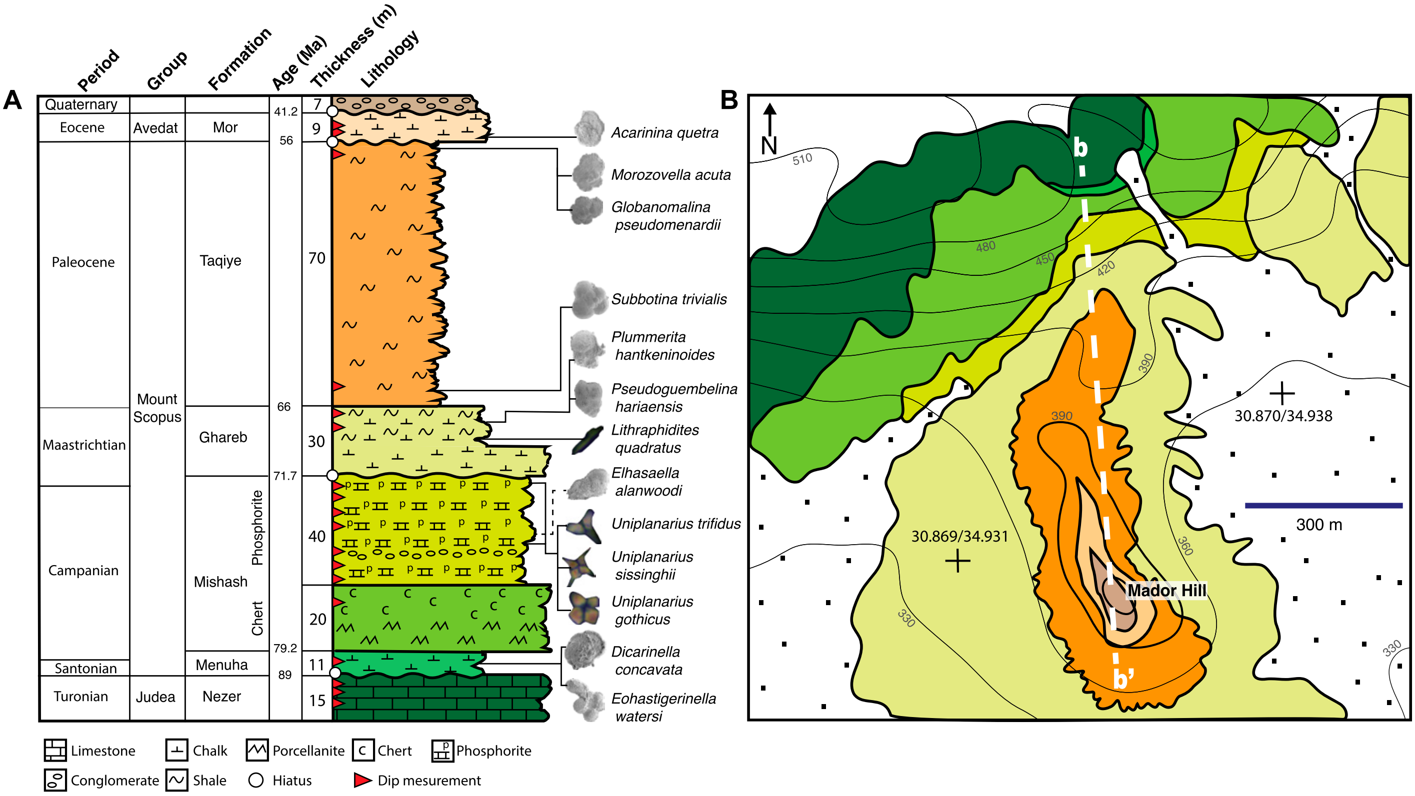

Figure 3. The investigated sedimentary sequence and detailed geological map. (A) Stratigraphical column of the investigated sedimentary section with notable biostratigraphic markers denoted at their stratigraphic location. Dip measurement stratigraphic locations are denoted with red triangles and hiatuses with white circles. (B) Detailed geological map, adapted from Roded (1982), with the location of the investigated transect (Fig. 4) shown by the dashed b–b′ white line.

nate from the chronostratigraphies of Coccioni and Premoli Silva (2015) and Huber et al. (2008, 2017, 2022).

Using geochronological methods, we have dated a single limestone sample with multiple calcitic gastropod fossils, collected from the Nezer Formation, for which no previous geochronological dating has been done. Most Cretaceous gastropods originally precipitated their shells as aragonite, which commonly undergoes replacement by calcite during diagenesis (Brand, 1989). Consequently, U-Pb dating of such calcites typically records the timing of diagenetic recrystallization rather than primary shell formation. However, aragonite-to-calcite replacement in marine carbonates often occurs during early diagenesis (i.e., soon after deposition), particularly under shallow burial conditions (Marshall, 1992). Therefore, the U-Pb ages of the Cretaceous gastropods closely approximate the depositional age of the host strata. We have measured the U-Pb isotope ratios of the sample, along with several other isotopes, at the LaserChron Laboratory located in the Department of Earth and Environmental Sciences, Ben-Gurion University of the Negev, Beer Sheva, Israel. The laboratory consists of a RESOlution-SE 193 nm excimer laser coupled to a Nu Attom single collector inductively coupled plasma–mass spectrometer (ICP-MS). Laser ablation parameters were 100 μm spot size, a fluence of 2.5–3 J/cm^2, ablation time of 30 s, repetition rate of 8 Hz, and 20 s washout time for background measurement between ablations. The ICP-MS measured 100 sweeps per integration with dwell times of 200 μs for masses ^{202}Hg, ^{204}Pb, ^{208}Pb, ^{232}Th, and ^{238}U, 400 μs for ^{206}Pb, and 1000 μs for ^{207}Pb and ^{235}U. Data reduction was performed in Iolite v4 (Paton et al., 2011) using the VisualAge UComPbine data reduction scheme (Chew et al., 2014). For drift normalization and mass bias correction, every seven unknown samples were bracketed by reference materials using WC-1 Calcite (254.4 ± 6.4 Ma; Roberts et al., 2017) as primary standard, and two unpublished secondary standards (WPT, 11.3 ± 0.3 Ma, and UCSB436, 13 ± 0.5 Ma). While ^{207}Pb/^{206}Pb ratios were corrected using SRM NIST614 in a second distinct analysis session, we note that the results of the two sessions were virtually identical. ^{202}Hg was measured for reduction of ^{204}Hg interferences from ^{204}Pb in case a correction was required, but no ^{202}Hg was detected. The U-Pb isotope ratios and the U and Pb concentration values are presented in the Supplemental Material.[1] ^{232}Th was also measured during the analyses, but the measured concentrations were below the detection limit and therefore are not presented here.

Folding Rates

We have integrated the structural observations with the acquired ages to determine how folding rates evolved with time. We have applied Monte Carlo simulations to compute folding rates values and their associated uncertainties (Anastasio et al., 2021). For each data point (i.e., dip magnitude, age, and their associated uncertainties), we have assigned random values of dip magnitudes, sampled from a normal distribution within the uncertainty space, and an age, sampled from a uniform distribution over the whole age uncertainty. Once a random folding rate path was computed, the accumulated dip magnitude reached at the end of each simulated path was

[1]Supplemental Material. U-Pb isotope ratios and U, Th, and Pb concentrations used for geochronological analysis. Please visit https://doi.org/10.1130/GSAB.S.30359176 to access the supplemental material; contact editing@geosociety.org with any questions.

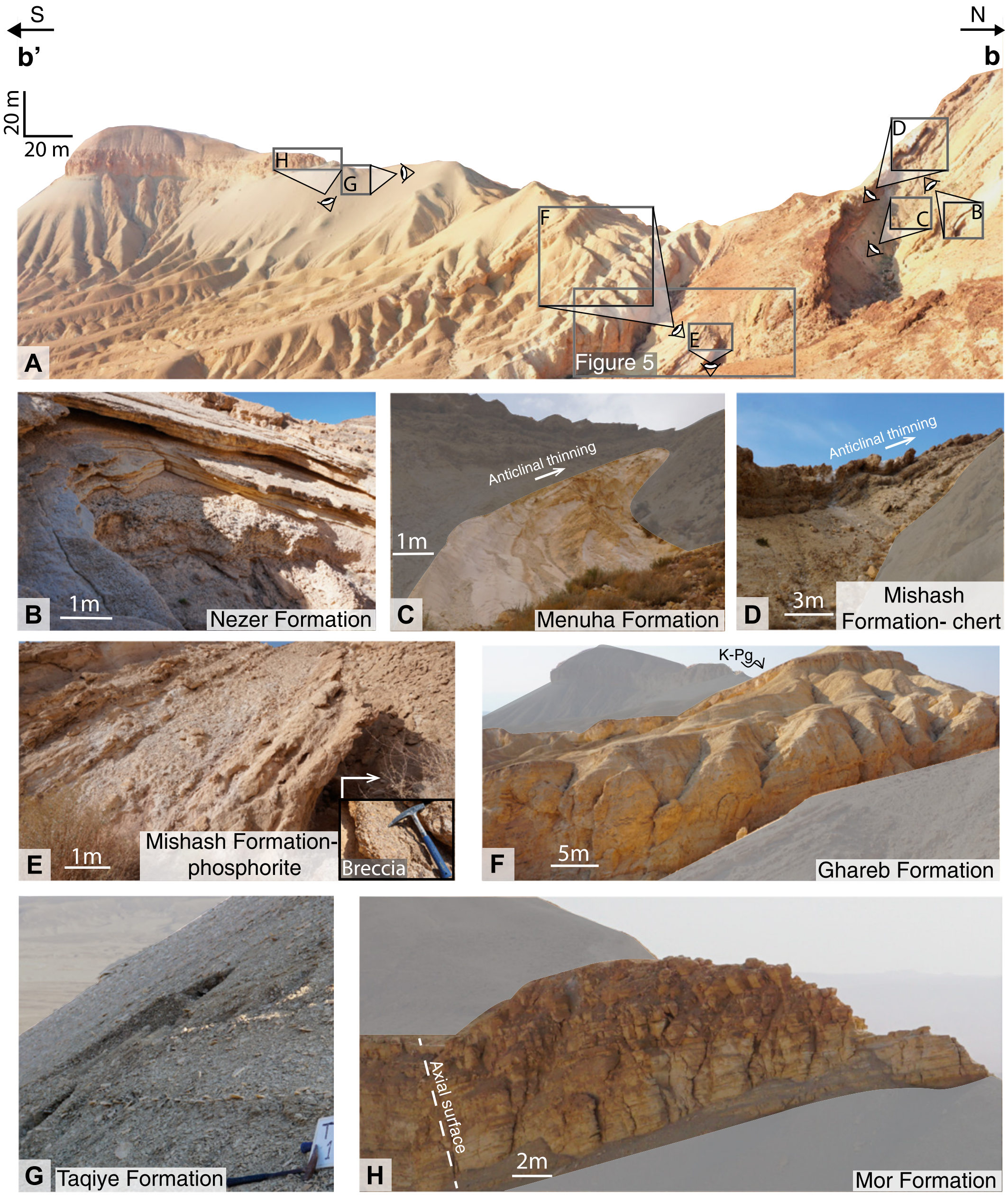

Figure 4. Representative field appearances of the various formations present at the investigated Mador Hill transect. (A) North-south view of the section, along the b–b′ transect (for location, see Fig. 3B). The locations of the representative views of the different formations (panels B–H) and of Figure 5 are shown with gray boxes. (B) Limestone of the Nezer Formation. (C) Chalks of the Menuha Formation. (D) Mishash chert and porcellanite member. The chert is overlaying the porcellanite unit. (E) Mishash phosphorite member. Bottom right inset: the breccia unit present within the member. (F) Ghareb Formation, a massive chalk unit overlain by a succession of chalk and shales. (G) Shales of the Taqiye Formation. (H) Chalk layers of the Mor Formation.

compared to the actual highest dip magnitude measured at the base of the section (i.e., 79.2° measured at the base of the structurally corrected Turonian Nezer Formation). If the observed and simulated dip angles were similar (i.e., within 10%), the simulated path was accepted. The calculated mean folding rate evolution path and its uncertainties were calculated based on 10,000 accepted simulations.

RESULTS

We have measured the orientation of 18 layers spread across the investigated section (Fig. 6 and Table 1). The observed dip magnitudes are generally decreasing up the section, with one notable exception found at the base of the section. There, the three older Nezer, Menuha, and Mishash Formations present low dip angles relative to the adjacent overlaid strata, suggesting that a local inflection, i.e., a change in the fold curvature (Nabavi and Fossen, 2021), exists (Fig. 6 and Table 1). Layers from the Mishash Formation are crossing the inflection continuously; thus, assuming that the inflection resulted in a constant change in dip magnitudes for the different levels of the strata, these Mishash layers document the effect of the inflection. To link the affected dip measurements of the oldest three formations with the rest of the section, we exploited the observed 29° change in dip magnitudes of the Mishash chert unit across the inflection. We have thus corrected the measured dip magnitudes of the lower three formations (Fig. 6C) by adding 29°.

In addition to the local deflection of the lowermost strata closest to the fold hinge, the structural position of the measurements with respect to the anticlinal axial surface (Fig. 2) may also affect the orientation of the layers. To evaluate this effect, we have continuously measured, at increasing distances from the fold hinge, the dip of the layer that has the longest exposure along the investigated transect, located in the center of the section, within the Ghareb Formation (high-

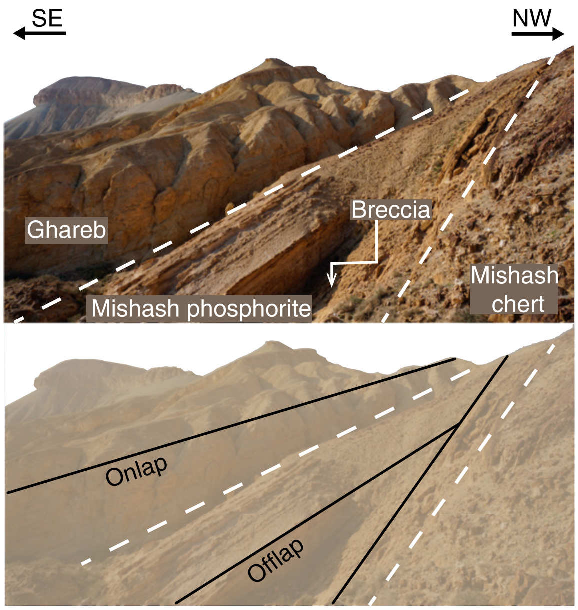

Figure 5. Field relationships between the Mishash and Ghareb Formations (see Fig. 4A for location). White lines in the upper panel highlight the locations of the boundaries between the different geological units, while the lower panel presents the same field photo, where the sedimentary interpreted structures are marked in black. The base of the phosphorite member is onlapping the older chert layers, followed by offlapping within the phosphorite member. The Maastrichtian Ghareb Formation is then onlapping the Mishash phosphorite member. A breccia layer (inset in Fig. 4E) is associated with this onlap-offlap transition.

lighted by a red arrow in Fig. 6B). The layer maintains a constant dip along the investigated part of the flank, showing no variations in orientation as a function of distance from the fold hinge. Thus, we assume that at the structural position that we investigate, each layer maintains a constant dip. Therefore, we did not perform structural correction for the strata located above the Mishash Formation chert unit and assumed that changes in orientations of the different layers reflect the shortening history rather than dip magnitude decrease due to increased distance from the hinge line.

The Taqiye shales mostly lack measurable strata. Fortunately, the base and top of the Taqiye Formation preserve measurable fine layers that are tilted at almost the same angle. Therefore, no shortening information is lost despite the absence of measurable strata. The similar dip magnitudes maintained across the 150 m horizontal distance between the base and the top of the Taqiye Formation (Figs. 6 and 7) also strengthens our assumption that the structural position (i.e., distance from the fold hinge) of our measurements has minimal impact on the orientation of the layers.

Our observations show that the first distinct dip magnitude change occurs at the Turonian, after which dip magnitude gradually decreases upward, indicating that folding started during the Turonian and lasted until at least the Lower Eocene (Fig. 7). The oldest sharp angular

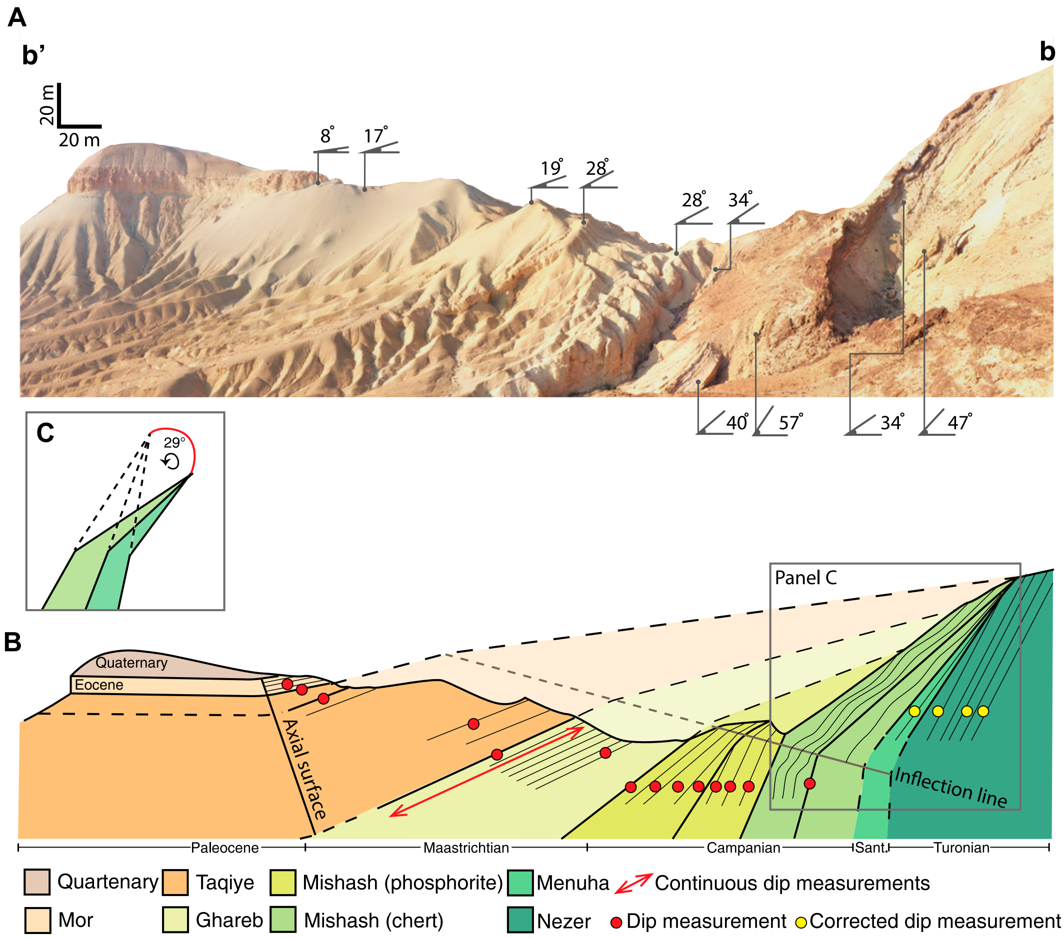

Figure 6. A view of the southern flank of the Hatira monocline, shown along the Mador Hill b–b′ transect (Fig. 3B). (A) Selected dip magnitudes of representative layers shown on top of a field photo. (B) Schematic illustration of the geological setting along the b–b′ transect shown in panel A. The sedimentary formations are color-coded. Interpreted structural and lithological transitions are marked with dashed lines. Circles mark the positions where structural measurements were taken. Red circles highlight the locations where no structural correction was made, while yellow circles highlight the locations where structural correction was applied. The red arrow denotes the well-exposed layer within the Ghareb Formation that was used to constrain the structural setting of the flank. Gray rectangle highlights the portion of the section that was structurally corrected (panel C). (C) Schematic representation of the correction used to adjust the inflected lower part of the strata.

TABLE 1. BIOSTRATIGRAPHICAL AND STRUCTURAL RESULTS FROM THE MADOR HILL SECTION (NEGEV DESERT, ISRAEL)

Formation	Lithology	Dip magnitude (°)	Corrected dip magnitude (°)	Measurement method	Biomarkers	Biozone
Mor	Chalk	8	8	Brunton	—	—
Mor	Chalk	10	10	Brunton	*Acarinina. esnaensis* *Acarinina quetra*	E3–E6 (Pearson et al., 2006)
Taqiye	Marl	17	17	Total Station	*Morozovella acuta* *Globanomalina pseudomenardii*	P4 (Wade et al., 2011)
Taqiye	Marl	19	19	Total Station	*Subbotina trivialis*	P1 (Wade et al., 2011)
Ghareb	Marly chalk	28.6	28.6	Total Station	—	—
Ghareb	Marly chalk	28.7	28.7	Total Station	*Plummerita hantkeninoides* *Pseudoguembelina hariaensis*	CF3 (Li and Keller, 1998)
Ghareb	Marly chalk	—	—	—	*Lithraphidites quadratus*	UC20a (Burnett, 1998)
Mishash	Phosphorate	34	34	Brunton	*Uniplanarius gothicus* *Uniplanarius sissinghii* *Uniplanarius trifidus*	UC15d (Burnett, 1998)
Mishash	Phosphorate	36	36	Brunton	—	—
Mishash	Phosphorate	38	38	Brunton	—	—
Mishash	Phosphorate	36.8	36.8	Brunton	—	—
Mishash	Phosphorate	—	—	—	*Elhasaella alanwoodi*	First occurrence at 76.2 Ma (Meilijson et al., 2014)
Mishash	Phosphorate	40.4	40.4	Brunton	*Uniplanarius gothicus* *Uniplanarius sissinghii* *Uniplanarius trifidus*	UC15d (Burnett, 1998)
Mishash	Phosphorate	50	50	Brunton	—	*Calochortus plummerae* (Meilijson et al., 2014)
Mishash	Phosphorate	57.9	57.9	Brunton	—	*Calochortus plummerae* (Meilijson et al., 2014)
Mishash	Chert	63/34	63	Brunton	—	*Calochortus plummerae* (Meilijson et al., 2014)
Menuha	Chalk	42	71	Total Station	*Dicarinella concavata* *Eohastigerinella watersi*	*Dicarinella asymetrica* (Caron, 1985)
Nezer	Limestone	47	76	Brunton	—	T7–Ca1 (Buchbinder et al., 2000)
Nezer	Limestone	49	78.2	Brunton	—	T7–Ca1 (Buchbinder et al., 2000)
Nezer	Limestone	50	79	Brunton	—	T7–Ca1 (Buchbinder et al., 2000)

Note: Dip magnitudes and their adjustments are presented. The main biomarkers and their biozones are indicated, as well as biozones inferred from lithological formations and previous works (Buchbinder et al., 2000; Meilijson et al., 2014). Dashes indicate layers in which either dip magnitudes or biostratigarphical samples were not collected.

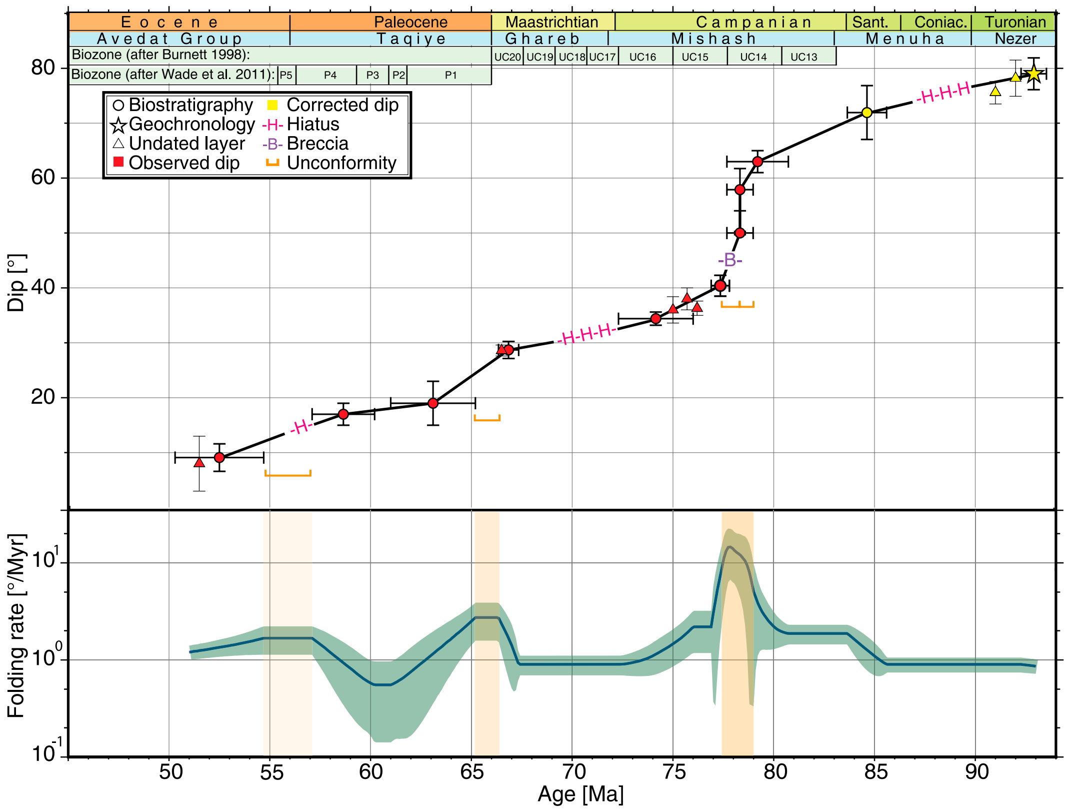

Figure 7. Folding evolution of the Hatira monocline. The upper panel shows the dip measurements and dating results. The geological periods, rock formations, and the global biozones used for biostratigraphical dating (Burnett, 1998; Wade et al., 2011) are shown at the top of the panel. Circles denote samples dated with biostratigraphy. Star denotes the sample dated with geochronology. Triangles highlight the layers to which only dip measurements were taken; thus, their ages are based on linear interpolation of the closest dated layers. Yellow-filled symbols highlight data whose dip magnitudes were structurally corrected, while red-filled symbols highlight data whose dip magnitudes were not structurally corrected. Stratigraphic hiatuses and the breccia layer are marked with the letters "H" and "B," respectively. Major unconformities are marked with orange horizontal bars. The lower panel shows the folding rates (note the logarithmic scale) calculated based on the data shown in the upper panel. Green area marks the 1σ confidence. Vertical orange bars highlight the episodes that experienced intense folding.

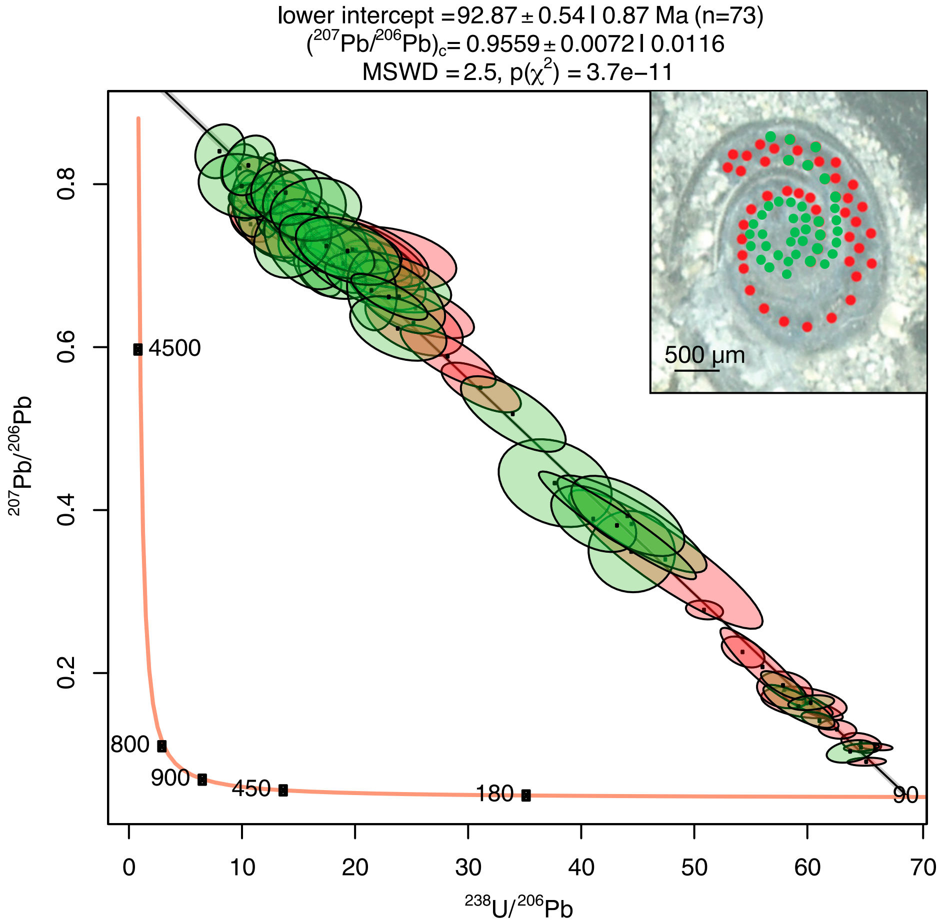

Figure 8. U-Pb geochronological results of sample G-4b shown on a Tera-Wasserburg concordia plot. Ellipses, showing the 2σ uncertainties, depict the two distinct analysis laboratory sessions where in the first session (green ellipses) an additional standard was used to correct Pb ratios. Red ellipses marked the results collected during the second session. Upper right inset presents the analyzed 73 spots colored according to the laboratory sessions. MSWD—mean square of weighted deviates.

unconformities (7.9° and 9.6°), which account for >20% of the accumulated folding, are found within the phosphorite member of the Mishash Formation across three adjacent layers. This abrupt change of dip magnitudes, in a period of relatively constant sedimentation rates (Meilijson et al., 2014), is accompanied by a sedimentary onlap to offlap depositional geometry and a breccia layer (Figs. 4E and 5). These observations indicate that high folding rates prevailed during the deposition of these strata (Hardy and Poblet, 1994). Two additional angular unconformities of ~9° were measured at the interface of both the Ghareb-Taqiye and Taqiye-Mor Formations. These two unconformities are accompanied by sedimentary facies changes, from chalk in the Ghareb Formation to the shales of the Taqiye Formation, and from the shales of the Taqiye Formation to the chalk of the Mor Formation. The latter unconformity is associated with an ~2 m.y. hiatus. The uppermost Lower Eocene layers have dip magnitudes of ~10°, indicating that younger (i.e., post–Lower Eocene) folding has most likely occurred. The lack of younger marine sediments prevents us from documenting the timing and style of post–Lower Eocene shortening.

Geochronological analysis of the sample from the Nezer Formation (i.e., marking the base of the section) yielded an age of 92.87 ± 0.54 Ma (Fig. 8). The U-Pb age is derived from the calcitic gastropod shell and is interpreted as reflecting early diagenesis, when the aragonite-to-calcite replacement occurs (Marshall, 1992). Given the analytical uncertainty associated with the U-Pb method (±0.54 m.y.), the age of calcite crystallization overlaps with the expected stratigraphic age of the host layer (Buchbinder et al., 2000). Our biostratigraphical analysis is based on 47 field samples and yielded 14 biomarkers, spanning 13 biozones (Fig. 3 and Table 1), resulting in a total of 10 biostratigraphic ages. The combination of various biostratigraphic taxonomical groups allowed us to cross-validate the dating results. The Santonian strata were dated with *Eohastigerinella watersi* and *Dicarinella concavata*, which mark the *Dicarinella asymetrica* biozone (Huber et al., 2017). The first sharp angular unconformity was dated using calcareous nannofossils and benthic foraminifera. In particular, the presence of *Uniplanarius gothicus*, *Uniplanarius sissinghii*, and *Uniplanarius trifidus* indicate the UC15d biozone (Burnett, 1998); meanwhile, the first occurrence of *Elhasaella alanwoodi* suggests an age of 76.2 Ma (Meilijson et al., 2014). The unconformity between the Maastrichtian and the Paleocene was dated with the presence of *Lithraphidites quadratus*, which indicates biozone UC20a (Burnett, 1998), *Pseudoguembelina hariaensis*, and *Plummerita hantkeninoides*, whose presence indicates biozone CF3 (Li and Keller, 1998), in the Maastrichtian layers, and *Subbotina trivialis*, whose presence indicates biozone P1-P2 (Huber et al., 2017) in the Paleocene layers. Between the Paleocene and the Eocene, the unconformity was dated in the Paleocene with the presence of *Morozovella acuta* and *Globanomalina pseudomenardii*, which indicate biozone P4 (Wade et al., 2011). We dated the Eocene layers with the presence of *Acarinina esnaensis* and *Acarinina quetra*, ranging from the top of biozone E3 to biozone E6 (Berggren et al., 2006). Overall, our dating of the Mador Hill transect yielded 11 ages that resulted in a mean temporal resolution of 3–4 m.y. Five of the dated layers are concentrated within the Middle Campanian, thus providing especially high temporal resolution (<1 m.y.) at the time of the intense folding episode (Fig. 7).

The initial folding rate was slow (~1°/m.y.) and persisted for most of the section (Fig. 7). The Late Santonian strata document an increase to 1.85°/m.y. ± 0.4°/m.y. folding rate, followed by a sharp increase (up to 15°/m.y. ± 9°/m.y.) that lasted between ca. 79 Ma and ca. 77 Ma. This folding pulse ended when the folding rate gradually decreased between ca. 76 Ma and ca. 73 Ma to reach the background slow folding rate. Two additional smaller folding pulses may have operated at the Late Maastrichtian (ca. 67 Ma to ca. 66 Ma) and at the Paleocene-Eocene boundary (ca. 56 Ma to ca. 55 Ma). We note that the ages of the layers bounding these two unconformities are not well constrained. Nevertheless, as no hiatuses are observed at the same stratigraphical levels in the neighboring synclines (Honigstein et al., 2002; Shahar, 1967), we propose that these unconformities mark periods of elevated folding rates, albeit less intense than the Campanian folding episode. Finally, we note that we cannot rule out that the slow background folding might have been accommodated by additional rather short and minor folding pulses; for instance, the ~8° tilt difference between the Turonian (dip magnitude of 79°) and the Santonian (dip magnitude of 71°) strata could also potentially have been formed by a folding pulse. Nevertheless, the large (9 m.y.) temporal span between these two dip measurements is accompanied by a regional hiatus (Buchbinder et al., 2000); thus, the folding rate that prevailed during this period is clouded with uncertainties. If indeed additional undocumented minor folding pulses have occurred, they are most likely masked due to sedimentation rates that are not sufficient to preserve the details of the shortening history and/or by hiatuses that led to sedimentary age gaps.

DISCUSSION AND CONCLUSIONS

The folding history of the Hatira monocline suggests that starting in the Late Cretaceous, a long-lasting slow shortening prevailed for at least 40 m.y. This background folding accommodated roughly half of the total shortening and was punctuated by a prominent folding pulse (ca. 79 Ma to ca. 77 Ma) and two rather minor pulses (at ca. 67 Ma to ca. 65 Ma and ca. 57 Ma to ca. 54 Ma). Folding activity between the Late Cretaceous and the Eocene has previously been identified along most of the arc, from the Palmyrides (Chaimov et al., 1992; Salel and Séguret, 1994), through the Negev Desert, Israel (Hardy et al., 2010), to Sinai, Egypt (Bosworth et al., 1999). While the folding pulses that we have uncovered in the Hatira monocline seem to have also been identified at other locations along the arc (Bosworth et al., 1999; Moustafa and Khalil, 1995; Salamon, 1987; Salel and Séguret, 1994; Walley, 1998), these studies had rather low temporal resolution as they mostly used the boundaries between the different stratigraphic formations to constrain the evolution of the folds. This knowledge gap, in turn, prevents us from assessing the evolution of the arc in time and space.

The high-resolution reconstruction of folding rates presented here unravels the 40 m.y. shortening history of the Hatira monocline, central Syrian Arc. As the major folding pulses observed are not associated with sharp changes in rheology or sedimentation rates (Meilijson et al., 2014), we propose that local basin-scale effects, such as sedimentary loading, could only play a minor role in the evolution of the Hatira monocline. Previous investigations proposed that a far-field stress regime controlled the development of the Syrian Arc (Eyal, 1996; Eyal and Reches, 1983), and the likely driver to induce these stresses is the northern African-Eurasian convergence plate boundary (e.g., Gianni et al., 2025; Şengör and Stock, 2014).

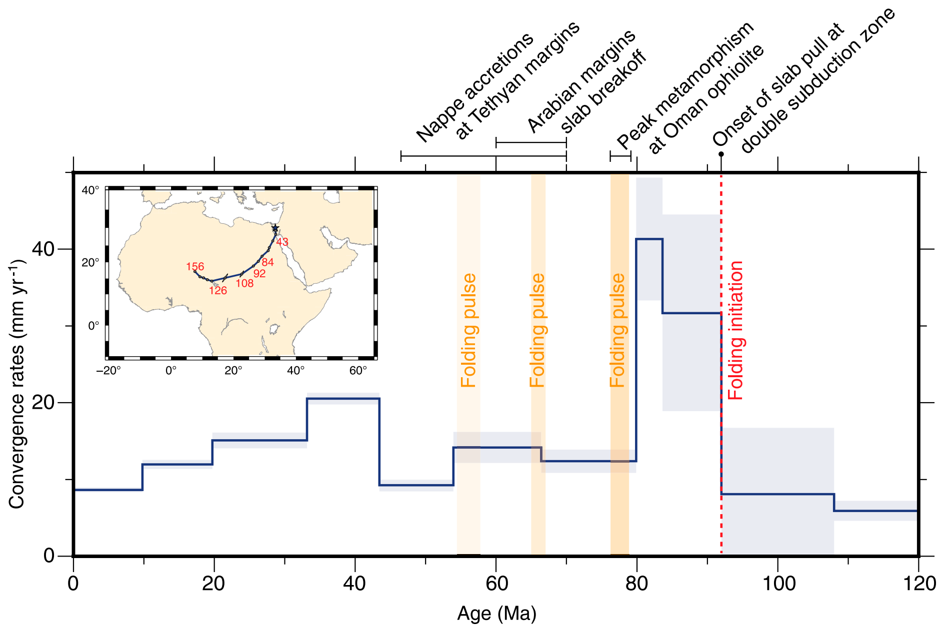

Figure 9. Africa-Eurasia relative plate motions during the past 120 m.y. Convergence rates (i.e., plate motion in the north-south direction) were computed based on the Africa trajectory shown in the inset. Shadings show the 1σ uncertainties of the convergence rates. A simplified representation of the major folding history of the Hatira monocline is denoted within the plot (based on the results presented in Fig. 7). Regional geodynamic events that occurred along the eastern part of the northern margin of Africa are marked at the top. The numbers in the inset highlight the ages in Ma along the calculated African trajectory. Calculation was based on the Euler pole parameters presented in Gürer et al. (2022).

The various time scales in which folding occurred hint at different geodynamic processes that may have induced shortening (Fig. 9). The initiation of shortening during the Turonian temporally coincided with a major Africa-Eurasia relative plate motion change, whereby convergence motion rapidly accelerated in northeastern Africa at ca. 92 Ma due to the emergence of a strong slab pull force induced by the northern Tethys double subduction zone system (Gürer et al., 2022; Fig. 1). Numerical modeling presented recently by Gianni et al. (2025) suggested that the northern double subduction zone system may have induced the driving compressional intraplate stresses that drove the initiation of shortening along the Syrian Arc. The major Campanian folding pulse, between ca. 79 Ma and ca. 77 Ma, coincided with a period of a sharp Africa-Eurasia deceleration of convergence rates, possibly related to the arrest of the Tethyan double subduction system (Gürer et al., 2022). This period also coincided with a metamorphism peak of the Cretaceous Tethyan ophiolites (specifically at the Oman ophiolite, Fig. 1C, at ca. 79 Ma), which was suggested to mark their emplacement onto the continental margins (Warren et al., 2005). Interestingly, the duration of the Tethyan ophiolite obduction process was on the order of 10–15 m.y. (Warren et al., 2005), possibly corresponding to the elevated folding rates that prevailed prior to and after this folding pulse. The two younger folding pulses could be temporally correlated to several processes occurring along the convergence front. The Late Maastrichtian (i.e., ca. 67 Ma to ca. 65 Ma) folding pulse is temporally correlated with a slab breakoff that occurred along the northern Arabian Plate margin (Agard et al., 2011), i.e., the Mesopotamian slab (van der Meer et al., 2018). Additionally, from the Maastrichtian to the Eocene, several accretions of continental nappes occurred along the northern Tethyan margin (van Hinsbergen et al., 2020, and references therein), now exposed in Turkey (Fig. 1C). These continental accretions might have induced intraplate compressional stresses onto the trailing African plate. Alternatively, the intraplate shortening might have been driven by processes occurring at the leading down-going subducting oceanic slab. For instance, slab buckling (van der Wiel et al., 2024), or plume-push (Jolivet et al., 2016) might have induced compressional intraplate stresses. While intriguing, because our work presents the history of shortening of a single fold structure, and because the temporal resolution of the existing African-Eurasian plate kinematic models is rather crude (Fig. 9), correlating the observed shortening history to specific geodynamic drivers is still highly speculative.

Overall, plate boundary conditions, plate kinematics, and local structural crustal weaknesses interact in a complex manner to form the observed intraplate shortening. Our results open new avenues for improving the understanding of the governing processes and forces acting at the confining plate boundaries and within the trailing continental lithosphere. Further investigation of other fold structures along the Syrian Arc, a new generation of high-temporal resolution plate kinematic models, and new geodynamical numerical simulations are needed to unravel the relative importance of the governing geodynamic processes acting in the subduction environment.

ACKNOWLEDGMENTS

This study is supported by Israeli Science Foundation grant 1923/21. G. Fisch is also supported by the Israeli Ministry of Energy fellowship program (grant 8102861). We thank Associate Editor Stefano Mazzoli and the two anonymous reviewers for their constructive and helpful reviews.

REFERENCES CITED

Agard, P., Omrani, J., Jolivet, L., Whitechurch, H., Vrielynck, B., Spakman, W., Monié, P., Meyer, B., and Wortel, R., 2011, Zagros orogeny: A subduction-dominated process: Geological Magazine, v. 148, p. 692–725, https://doi.org/10.1017/S001675681100046X.

Almogi-Labin, A., Bein, A., and Sass, E., 1993, Late Cretaceous upwelling system along the Southern Tethys Margin (Israel): Interrelationship between productivity, bottom water environments, and organic matter preservation: Paleoceanography, v. 8, p. 671–690, https://doi.org/10.1029/93PA02197.

Anastasio, D.J., Kodama, K.P., Parés, J.M., Hinnov, L.A., and Idleman, B.D., 2021, Internal and external modulation of folding rates with 10^4 to 10^5 year time resolutions from growth strata, Pico del Aguila, Spain: Geochemistry, Geophysics, Geosystems, v. 22, https://doi.org/10.1029/2021GC009828.

Ashckenazi-Polivoda, S., Titelboim, D., Meilijson, A., Almogi-Labin, A., and Abramovich, S., 2018, Bathymetric trend of Late Cretaceous southern Tethys upwelling regime based on benthic foraminifera: Cretaceous Research, v. 82, p. 40–55, https://doi.org/10.1016/j.cretres.2017.10.014.

Avni, Y., 1989, The geology, paleogeography and the evolution of the landscape in the central Negev highlands and the western Ramon ridge [M.Sc. thesis]: Jerusalem, The Hebrew University of Jerusalem, 300 p.

Berggren, W.A., Pearson, P.N., Huber, B.T., and Wade, B.S., 2006, Taxonomy, biostratigraphy, and phylogeny of Eocene Acarinina, *in* Pearson, P.N., Olsson, R.K., Huber, B.T., Hemleben, C., and Berggren, W.A., eds., Atlas of Eocene Planktonic Foraminifera: Cushman Foundation for Foraminiferal Research Special Publication 41, p. 257–326.

Bosworth, W., Guiraud, R., and Kessler, L.G., II, 1999, Late Cretaceous (ca. 84 Ma) compressive deformation of the stable platform of northeast Africa (Egypt): Far-field stress effects of the "Santonian event" and origin of the Syrian Arc deformation belt: Geology, v. 27, p. 633–636, https://doi.org/10.1130/0091-7613(1999)027<0633:LCCMCD>2.3.CO;2.

Bown, P.R., 1998, Calcareous Nannofossil Biostratigraphy: Kluwer Academic Publishers, 315 p.

Bown, P.R., and Young, J.R., 1998, Techniques, *in* Bown, P.R., ed., Calcareous Nannofossil Biostratigraphy: Kluwer Academic Publishers, p. 16–28.

Brand, U., 1989, Aragonite-calcite transformation based on Pennsylvanian molluscs: Geological Society of America Bulletin, v. 101, p. 377–390, https://doi.org/10.1130/0016-7606(1989)101<0377:ACTBOP>2.3.CO;2.

Buchbinder, B., Benjamini, C., and Lipson-Benitah, S., 2000, Sequence development of Late Cenomanian–Turonian carbonate ramps, platforms and basins in Israel: Cretaceous Research, v. 21, p. 813–843, https://doi.org/10.1006/cres.2000.0228.

Burnett, J.A., 1998, Upper Cretaceous, *in* Bown, P.R., ed., Calcareous Nannofossil Biostratigraphy: Kluwer Academic Publishers, p. 132–199.

Caron, M., 1985, Cretaceous Planktonic foraminifera, *in* Bolli, H.M., Saunders, J.B., and Perch-Nielsen, K., eds., Plankton Stratigraphy, Volume 1: Planktic Foraminifera, Calcareous Nannofossils and Calpionellids: Cambridge, UK, Cambridge University Press, Cambridge Earth Science Series, p. 17–86.

Chaimov, T.A., Barazangi, M., Al-Saad, D., Sawaf, T., and Gebran, A., 1992, Mesozoic and Cenozoic deformation inferred from seismic stratigraphy in the southwestern intracontinental Palmyride fold-thrust belt, Syria: Geological Society of America Bulletin, v. 104, p. 704–715, https://doi.org/10.1130/0016-7606(1992)104<0704:MACDIF>2.3.CO;2.

Chew, D.M., Petrus, J.A., and Kamber, B.S., 2014, U–Pb LA–ICPMS dating using accessory mineral standards with variable common Pb: Chemical Geology, v. 363, p. 185–199, https://doi.org/10.1016/j.chemgeo.2013.11.006.

Coccioni, R., and Premoli Silva, I., 2015, Revised Upper Albian–Maastrichtian planktonic foraminiferal biostratigraphy and magnetostratigraphy of the classical Tethyan Gubbio section (Italy): Newsletters on Stratigraphy, v. 48, no. 1, p. 47–90, https://doi.org/10.1127/nos/2015/0055.

Eyal, Y., 1996, Stress field fluctuations along the Dead Sea rift since the middle Miocene: Tectonics, v. 15, p. 157–170, https://doi.org/10.1029/95TC02619.

Eyal, Y., and Reches, Z.e., 1983, Tectonic analysis of the Dead Sea Rift Region since the Late-Cretaceous based on mesostructures: Tectonics, v. 2, p. 167–185, https://doi.org/10.1029/TC002i002p00167.

Flexer, A., 1968, Stratigraphy and facies development of Mount Scopus Group (Senonian-Paleocene) in Israel and adjacent countries: Israel Journal of Earth Sciences, v. 17, no. 3, p. 85–114.

Flexer, A., 1971, Late Cretaceous paleogeography of northern Israel and its significance for the Levant geology: Palaeogeography, Palaeoclimatology, Palaeoecology, v. 10, p. 293–316, https://doi.org/10.1016/0031-0182(71)90053-8.

Frizon de Lamotte, D., Raulin, C., Mouchot, N., Wrobel-Daveau, J.-C., Blanpied, C., and Ringenbach, J.-C., 2011, The southernmost margin of the Tethys realm during the Mesozoic and Cenozoic: Initial geometry and timing of the inversion processes: Tectonics, v. 30, https://doi.org/10.1029/2010TC002691.

Gardosh, M.A., Garfunkel, Z., Druckman, Y., and Buchbinder, B., 2010, Tethyan rifting in the Levant Region and its role in Early Mesozoic crustal evolution, *in* Homberg, C., and Bachmann, M., eds., Evolution of the Levant Margin and Western Arabia Platform since the Mesozoic: Geological Society, London, Special Publication 341, p. 9–36, https://doi.org/10.1144/SP341.2.

Garfunkel, Z., 2004, Origin of the Eastern Mediterranean basin: A reevaluation: Tectonophysics, v. 391, p. 11–34, https://doi.org/10.1016/j.tecto.2004.07.006.

Gianni, G.M., Guo, Z., Holt, A.F., and Faccenna, C., 2025, Non-collisional orogeny in northeast Japan driven by nearby same-dip double subduction: Nature Geoscience, v. 18, p. 525–533, https://doi.org/10.1038/s41561-025-01704-5.

Granot, R., 2016, Palaeozoic oceanic crust preserved beneath the eastern Mediterranean: Nature Geoscience, v. 9, p. 701–705, https://doi.org/10.1038/ngeo2784.

Guiraud, R., and Bosworth, W., 1997, Senonian basin inversion and rejuvenation of rifting in Africa and Arabia: Synthesis and implications to plate-scale tectonics: Tectonophysics, v. 282, p. 39–82, https://doi.org/10.1016/S0040-1951(97)00212-6.

Gürer, D., Granot, R., and van Hinsbergen, D.J.J., 2022, Plate tectonic chain reaction revealed by noise in the Cretaceous quiet zone: Nature Geoscience, v. 15, p. 233–239, https://doi.org/10.1038/s41561-022-00893-7.

Hardy, C., Homberg, C., Eyal, Y., Barrier, É., and Müller, C., 2010, Tectonic evolution of the southern Levant margin since Mesozoic: Tectonophysics, v. 494, p. 211–225, https://doi.org/10.1016/j.tecto.2010.09.007.

Hardy, S., and Poblet, J., 1994, Geometric and numerical model of progressive limb rotation in detachment folds: Geology, v. 22, p. 371–374, https://doi.org/10.1130/0091-7613(1994)022<0371:GANMOP>2.3.CO;2.

Honigstein, A., Rosenfeld, A., and Benjamini, C., 2002, Eocene ostracode faunas from the Negev, southern Israel: Taxonomy, stratigraphy and paleobiogeography: Micropaleontology, v. 48, p. 365–389, https://doi.org/10.1661/0026-2803(2002)048[0365:EOFFTN]2.0.CO;2.

Huber, B.T., MacLeod, K.G., and Tur, N.A., 2008, Chronostratigraphic framework for upper Campanian–Maastrichtian sediments on the Blake Nose (subtropical North Atlantic): Journal of Foraminiferal Research, v. 38, p. 162–182, https://doi.org/10.2113/gsjfr.38.2.162.

Huber, B.T., Petrizzo, M.R., Young, J.R., Falzoni, F., Gilardoni, S.E., Bown, P.R., and Wade, B.S., 2017, Pforams@microtax: A new online taxonomic database for planktonic foraminifera: Micropaleontology, v. 62, no. 6, p. 429–438, https://doi.org/10.47894/mpal.62.6.02.

Huber, B.T., Tur, N.A., Self-Trail, J., and MacLeod, K.G., 2022, Calcareous plankton biostratigraphic fidelity and species richness during the last 10 m.y. of the Cretaceous at Blake Plateau, subtropical North Atlantic: Cretaceous Research, v. 131, https://doi.org/10.1016/j.cretres.2021.105095.

Jolivet, L., Faccenna, C., Agard, P., Frizon de Lamotte, D., Menant, A., Sternai, P., and Guillocheau, F., 2016, Neo-Tethys geodynamics and mantle convection: From extension to compression in Africa and a conceptual model for obduction: Canadian Journal of Earth Sciences, v. 53, p. 1–15, https://doi.org/10.1139/cjes-2015-0118.

Krenkel, E., 1924, Der Syrische Bogen: Zentralblatt für Mineralogie, v. 9, p. 274–281.

Li, L., and Keller, G., 1998, Maastrichtian climate, productivity and faunal turnovers in planktic foraminifera in South Atlantic DSDP sites 525A and 21: Marine Micropaleontology, v. 33, p. 55–86, https://doi.org/10.1016/S0377-8398(97)00027-3.

Marshall, J.D., 1992, Climatic and oceanographic isotopic signals from the carbonate rock record and their preservation: Geological Magazine, v. 129, no. 2, p. 143–160, https://doi.org/10.1017/S0016756800008244.

Meilijson, A., Ashckenazi-Polivoda, S., Ron-Yankovich, L., Illner, P., Alsenz, H., Speijer, R.P., Almogi-Labin, A., Feinstein, S., Berner, Z., Püttmann, W., and Abramovich, S., 2014, Chronostratigraphy of the Upper Cretaceous high productivity sequence of the southern Tethys, Israel: Cretaceous Research, v. 50, p. 187–213, https://doi.org/10.1016/j.cretres.2014.04.006.

Moustafa, A.R., and Khalil, S.M., 1995, Rejuvenation of the Tethyan passive continental margin of northern Sinai: Deformation style and age (Gebel Yelleq area): Tectonophysics, v. 241, p. 225–238, https://doi.org/10.1016/0040-1951(94)00167-8.

Nabavi, S.T., and Fossen, H., 2021, Fold geometry and folding—A review: Earth-Science Reviews, v. 222, https://doi.org/10.1016/j.earscirev.2021.103812.

Paton, C., Hellstrom, J., Paul, B., Woodhead, J., and Hergt, J., 2011, Iolite: Freeware for the visualisation and processing of mass spectrometric data: Journal of Analytical Atomic Spectrometry, v. 26, p. 2508–2518, https://doi.org/10.1039/c1ja10172b.

Reches, Z., Hoexter, D.F., and Hirsch, F., 1981, The structure of a monocline in the Syrian Arc system, Middle East-surface and subsurface analysis: Journal of Petroleum Geology, v. 3, p. 413–426, https://doi.org/10.1111/j.1747-5457.1981.tb00939.x.

Riba, O., 1976, Syntectonic unconformities of the Alto Cardener, Spanish Pyrenees: A genetic interpretation:

Sedimentary Geology, v. 15, p. 213–233, https://doi.org/10.1016/0037-0738(76)90017-8.

Roberts, N.M.W., Parrish, R.R., Smith, C.J., Horstwood, M.S.A., and Condon, D.J., 2017, A calcite reference material for LA-ICP-MS U-Pb geochronology: Geochemistry, Geophysics, Geosystems, v. 18, p. 2807–2814, https://doi.org/10.1002/2016GC006784.

Roded, R., 1982, The geological map of Israel: Israel Geological Survey, Jerusalem, Sheet 19-III: Oron, scale 1:50,000.

Sagy, Y., Gvirtzman, Z., and Reshef, M., 2018, 80 m.y. of folding migration: New perspective on the Syrian arc from Levant Basin analysis: Geology, v. 46, p. 175–178, https://doi.org/10.1130/G39654.1.

Salamon, A., 1987, The monoclines in the northern Negev: A model of tilted blocks and shortening [M.Sc. thesis]: Jerusalem, The Hebrew University of Jerusalem, 101 p.

Salel, J.F., and Séguret, M., 1994, Late Cretaceous to Palaeogene thin-skinned tectonics of the Palmyrides belt (Syria): Tectonophysics, v. 234, p. 265–290, https://doi.org/10.1016/0040-1951(94)90228-3.

Şengör, A.M.C., and Stock, J., 2014, The Ayyubid Orogen: An Ophiolite Obduction-Driven Orogen in the Late Cretaceous of the Neo-Tethyan South Margin: Geoscience Canada, v. 41, p. 225–254, https://doi.org/10.12789/geocanj.2014.41.042.

Shahar, J., 1967, The Ghareb formation in the Negev [M.Sc. thesis]: Jerusalem, The Hebrew University of Jerusalem, 109 p.

Shahar, J., 1994, The Syrian arc system: An overview: Palaeogeography, Palaeoclimatology, Palaeoecology, v. 112, p. 125–142, https://doi.org/10.1016/0031-0182(94)90137-6.

Shamir, G., and Eyal, Y., 1995, Elastic modeling of fault-driven monoclinal fold patterns: Tectonophysics, v. 245, no. 1, p. 13–24, https://doi.org/10.1016/0040-1951(94)00250-D.

Soudry, D., Nathan, Y., and Roded, R., 1985, The Ashosh-Haroz facies and their significance to the Mishash paleogeography and phosphorite accumulation in the northern and central Negev, southern Israel: Israel Journal of Earth Sciences, v. 34, p. 211–220.

Soudry, D., Glenn, C.R., Nathan, Y., Segal, I., and Vonder-Haar, D., 2006, Evolution of Tethyan phosphogenesis along the northern edges of the Arabian–African shield during the Cretaceous–Eocene as deduced from temporal variations of Ca and Nd isotopes and rates of P accumulation: Earth-Science Reviews, v. 78, p. 27–57, https://doi.org/10.1016/j.earscirev.2006.03.005.

Suppe, J., Chou, G.T., and Hook, S.C., 1992, Rates of folding and faulting determined from growth strata, *in* McClay, K.R., ed., Thrust Tectonics: Dordrecht, Netherlands, Springer, p. 105–121, https://doi.org/10.1007/978-94-011-3066-0_9.

van der Meer, D.G., van Hinsbergen, D.J.J., and Spakman, W., 2018, Atlas of the underworld: Slab remnants in the mantle, their sinking history, and a new outlook on lower mantle viscosity: Tectonophysics, v. 723, p. 309–448, https://doi.org/10.1016/j.tecto.2017.10.004.

van der Wiel, E., Pokorný, J., Čížková, H., Spakman, W., van den Berg, A.P., and van Hinsbergen, D.J.J., 2024, Slab buckling as a driver for rapid oscillations in Indian plate motion and subduction rate: Communications Earth & Environment, v. 5, 316, https://doi.org/10.1038/s43247-024-01472-x.

van Hinsbergen, D.J.J., Torsvik, T.H., Schmid, S.M., Maţenco, L.C., Maffione, M., Vissers, R.L.M., Gürer, D., and Spakman, W., 2020, Orogenic architecture of the Mediterranean region and kinematic reconstruction of its tectonic evolution since the Triassic: Gondwana Research, v. 81, p. 79–229, https://doi.org/10.1016/j.gr.2019.07.009.

Wade, B.S., Pearson, P.N., Berggren, W.A., and Pälike, H., 2011, Review and revision of Cenozoic tropical planktonic foraminiferal biostratigraphy and calibration to the geomagnetic polarity and astronomical time scale: Earth-Science Reviews, v. 104, p. 111–142, https://doi.org/10.1016/j.earscirev.2010.09.003.

Walley, C.D., 1998, Some outstanding issues in the geology of Lebanon and their importance in the tectonic evolution of the Levantine region: Tectonophysics, v. 298, p. 37–62, https://doi.org/10.1016/S0040-1951(98)00177-2.

Warren, C.J., Parrish, R.R., Waters, D.J., and Searle, M.P., 2005, Dating the geologic history of Oman's Semail ophiolite: Insights from U-Pb geochronology: Contributions to Mineralogy and Petrology, v. 150, p. 403–422, https://doi.org/10.1007/s00410-005-0028-5.

Zilberman, E., 2024, "Makhteshim"—Unique Arid Land Erosion Cirques in the Negev, *in* Frumkin, A., and Shtober-Zisu, N., eds., Landscapes and Landforms of Israel: Cham, Switzerland, Springer International Publishing, p. 297–311, https://doi.org/10.1007/978-3-031-44764-8_17.

Zur, Y., 1997, Unconformities associated with the development of Hatira monocline in the Giva't Mador area [M.Sc. thesis]: Beer Sheva, Israel, Ben-Gurion University of the Negev, 139 p.

Science Editor: Mihai Ducea
Associate Editor: Stefano Mazzoli

Manuscript Received 26 March 2025
Revised Manuscript Received 20 August 2025
Manuscript Accepted 19 September 2025